Available online at www.sciencedirect.com

SciVerse ScienceDirect

Acta Materialia 60 (2012) 4661–4671

Acta MATERIALIA

www.elsevier.com/locate/actamat

Confined recrystallization of high-purity aluminium during accumulative roll bonding of aluminium laminates

Paul Chekhonin [a], Benoît Beausir [a,b], Juliane Scharnweber [a], Carl-Georg Oertel [a], Tina Hausöl [c], Heinz Werner Höppel [c], Heinz-Günter Brokmeier [d], Werner Skrotzki [a,*]

[a] *Institut für Strukturphysik, Technische Universität Dresden, D-01062 Dresden, Germany*
[b] *Laboratoire d'Etude des Microstructures et de Mécanique des Matériaux (LEM3), UMR CNRS 7239, Université de Lorraine, Île du Saulcy, 57045 Metz Cedex 1, France*
[c] *Lehrstuhl Allgemeine Werkstoffwissenschaften, Universität Erlangen-Nürnberg, D-91058 Erlangen, Germany*
[d] *Helmholtz-Zentrum Geesthacht, D-21494 Geesthacht, Germany*

Received 9 March 2012; accepted 1 April 2012
Available online 10 May 2012

Abstract

Aluminium laminates consisting of high-purity aluminium and commercially pure aluminium have been produced by accumulative roll bonding (ARB) at ambient temperature for up to 10 cycles. To study the microstructure and texture development of the high-purity aluminium layers with regard to the shrinking layer thickness during ARB, microstructure and texture investigations were carried out by electron backscatter diffraction and neutron and X-ray diffraction, respectively. While the commercially pure aluminium layers develop an ultrafine-grained microstructure, partial discontinuous recrystallization occurs in the high-purity layers. The texture of the high-purity layers mainly consists of Cube and "Tilted Cube" (tilted with respect to the transverse direction) components. The experimental results are discussed with respect to confined recrystallization in the ARB aluminium laminates.

Keywords: Aluminium; Accumulative roll bonding; Laminates; Confined recrystallization; Texture

1. Introduction

Accumulative roll bonding (ARB) is a promising method for the production of ultrafine-grained (UFG) materials with grain sizes of <1 μm [1–6]. Due to their high specific strength, UFG sheets made by ARB have interesting mechanical properties. The relatively simple process allows the production of composites with sheets of different materials or ready-prepared sandwiches [7–19]. Because the geometry of the sheets does not change by applying ARB, any amount of deformation and any number of layers in composites can be theoretically achieved by this process.

So far, the majority of research on ARB and ARB composites has been done on materials that do not recrystallize discontinuously during or after processing. To produce an UFG structure, discontinuous recrystallization is of course undesirable. Nevertheless, or even more because of that reason, the mechanism and kinetics of recrystallization have to be studied thoroughly. Several authors have analyzed the recrystallization in ARB composites during annealing [10,11,14,15]. However, in these investigations recrystallization was achieved statically and only a limited range of layer thicknesses was analyzed. Therefore, it is the objective of the present work to investigate multilayered sheets composed of two distinct materials. The first is commercially pure aluminium developing a refined microstructure during ARB by continuous dynamic recrystallization [6]. The second is high-purity aluminium, which is known to show discontinuous dynamic recrystallization at ambient temperature [20,21] and slightly elevated temperatures [22,23]. By applying up to 10 ARB cycles, layer thicknesses

---

[*] Corresponding author.
E-mail address: werner.skrotzki@physik.tu-dresden.de (W. Skrotzki).

1359-6454/$36.00 © 2012 Acta Materialia Inc. Published by Elsevier Ltd. All rights reserved.
http://dx.doi.org/10.1016/j.actamat.2012.04.004

from 500 μm to 1 μm were produced and analyzed. The present investigation focuses on the recrystallization behaviour of the high-purity aluminium under spatial confinement. The microstructure and texture development of the high-purity layers is analyzed in detail and compared with results from static annealing investigations. The results on the layers of the commercially pure aluminium will be presented in a separate paper [24].

2. Experimental details

Sheets of high-purity aluminium (5 N or 99.999 wt.% Al, labelled **P** for "Pure") and of commercially purity aluminium (99.5 wt.% Al, labelled **A** for "Alloy") with a thickness of 1 mm each, were annealed at 500 °C for 1 h. After wire brushing the sheets were roll bonded at ambient temperature by a four-high rolling mill (Carl Wezel, Mühlacker) with a pass reduction of 50%. The rolls had a diameter of 32 mm, the rolling speed was 8 m min^{-1} and no lubrication was used. The rolling direction of the sheets was maintained throughout all the rolling passes. From the starting stack, consisting of one A and one P layer, 1–10 ARB cycles produced sheet samples with an asymmetric through-thickness distribution. With the A-layer always on the top and the P-layer on the bottom of the sheet (Fig. 1), the composites are labelled as AP#, where # is the number of the applied cycles.

Depending on the number of cycles, the layer thickness of the P-layers varied between about 0.5 mm after the first cycle and about 1 μm after 10 cycles. The investigation of the microstructure was carried out through backscatter electron (BSE) imaging and electron backscatter diffraction (EBSD) in a Zeiss ULTRA 55 scanning electron microscope on planes normal to the transverse direction (TD) and rolling direction (RD). The automatic indexing of the Kikuchi pattern was done by the software Channel 5 (HKL Technology). For analysis of the orientation maps the software EBSDmcf [25] was used, and the BSE images were evaluated using the software SmartTIFF (Carl Zeiss SMT). Specimen preparation for scanning electron microscopy (SEM) and EBSD investigations was done by mechanical grinding (final step: wet SiC-paper 2400 grid) and electropolishing using 9 vol.% perchloric acid in 91 vol.% ethanol at −13 °C and at 42 V polishing voltage. Global texture measurements were done by neutron diffraction [26] on cubes of stacked sheets (1 cm × 1 cm × 1 cm). Local texture measurements were performed using a HZG-4 X-ray texture diffractometer on the normal direction (ND) planes of the sheets. By grinding the sheets on their ND plane the texture at a certain depth could be captured by X-ray diffraction. To describe the measurement (thickness) position the parameter s is introduced, with $s = 0$, 0.5 and 1 referring to the top, middle and bottom of the sheet, respectively (Fig. 1). (1 1 1), (2 0 0) and (2 2 0) pole figures were measured by neutron and X-ray diffraction (complete and incomplete), respectively. The orientation distribution function (ODF) was calculated with the software Labotex (Labosoft) using the arbitrary defined cells method.

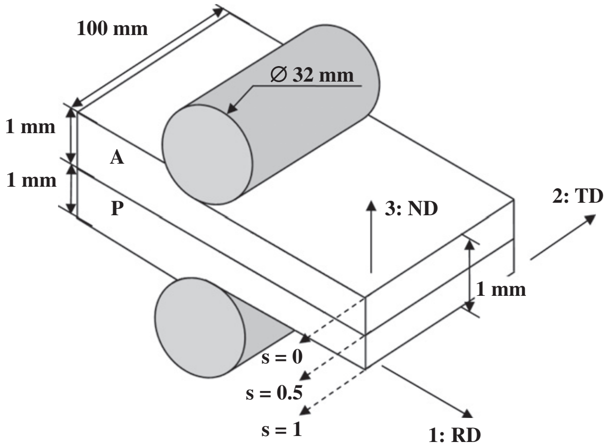

Fig. 1. Sketch of the first ARB cycle. The parameter s describes the thickness position.

3. Results

3.1. Microstructure

Fig. 2a and b shows BSE images of fully recrystallized initial microstructures for both materials. The initial grain size of the commercially pure aluminium is about 23 μm in RD and 14 μm in ND [6,27]. In Fig. 2b two exemplars of the high-purity sheets are shown. The bottom part of Fig. 2b shows a grain size between a few hundred micrometers to about 1 mm. The sheet in the upper part of Fig. 2b shows only one orientation (also confirmed by EBSD measurements), so tertiary recrystallization must have occurred while annealing. During ARB a layered structure develops, consisting of parallel aligned commercially pure (A) layers and high-purity (P) layers. A detailed analysis of the development of a UFG microstructure in the A-layers will be presented in Ref. [24].

The microstructure in the P-layers changes during ARB due to deformation and discontinuous recrystallization. After the first ARB cycle, deformed grains of typical laminar structure with subgrains can be seen in the P-layers as well as recrystallized areas (Figs. 2c and 3). Especially near the laminate boundaries the pure aluminium is completely recrystallized.

In Fig. 3 the orientation contrast after 1 cycle is shown comparing the orientation of each point of the mapping with the ideal orientations of both the rolling and recrystallization texture components of face-centred cubic (fcc) metals given in Table 1. The colour corresponds to that ideal orientation with which the disorientation has the smallest value (if a limit of 25° is exceeded for all given ideal orientations, the band contrast is plotted on a grey scale). With increasing deviation from the ideal orientation the colour fades to white. For all ideal orientations in Table

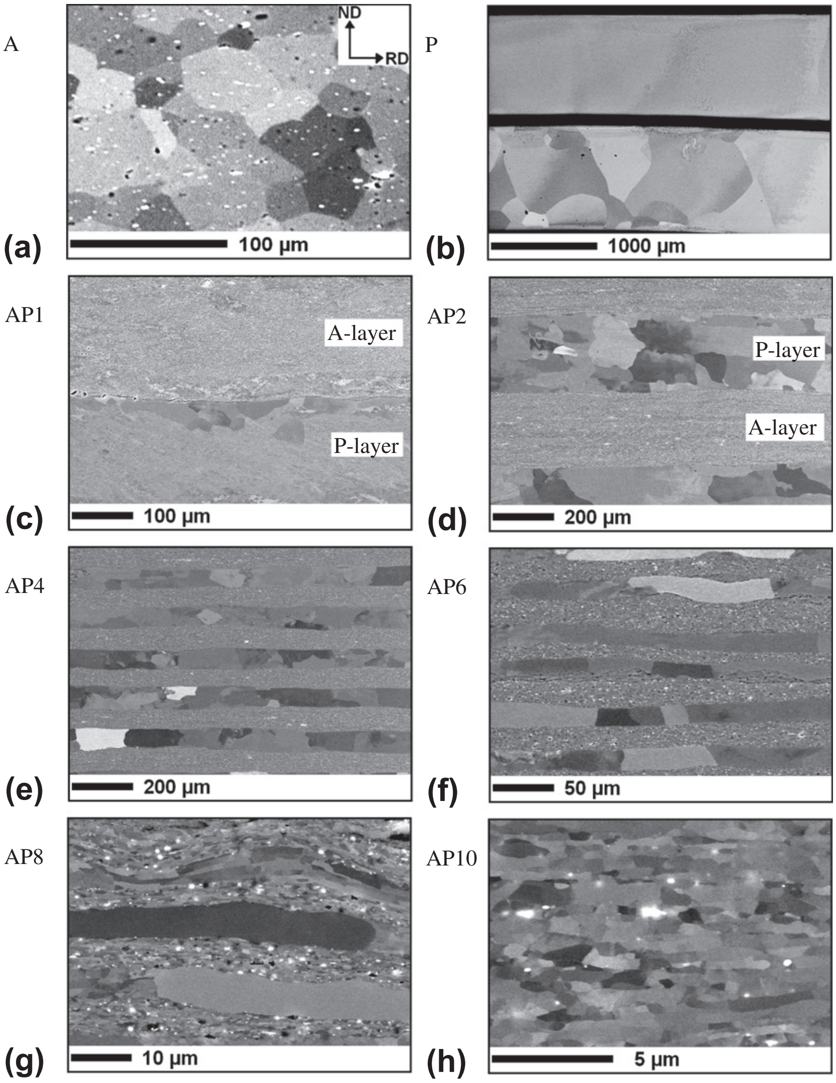

Fig. 2. BSE images of the initial materials: (a) commercial-purity and (b) high-purity aluminium and ARB composites after (c) 1, (d) 2, (e) 4, (f) 6, (g) 8 and (h) 10 cycles.

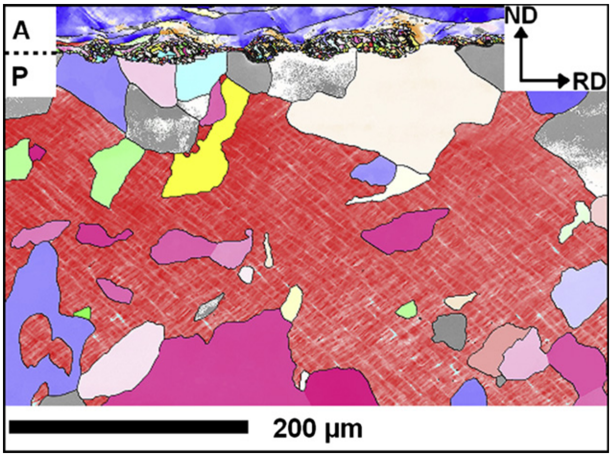

Fig. 3. Orientation map after 1 cycle ($0.47 < s < 0.80$; step size = 0.5 µm) obtained by EBSD, the colour code is given in Table 1.

Table 1
Colour coding of selected ideal orientations with corresponding Euler angles.

Colour	Name (acronym)	φ_1	Φ	φ_2
🟦	Cube (Cube)	45	0	45
🟩	Brass (Bs)	54.74	90	45
🟨	S (S)	58.98	36.7	63.43
🟥	Copper (Cu)	90	35.26	45
🟪	Goss (G)	90	90	45
🟦	Rotated Cube (C)	0	0	45
🟧	Rotated Goss (RG)	0	90	45
0° (disorientation) 25°				

1, the symmetric orientations considering orthorhombic specimen symmetry are included. Consequently, there are two crystallographically different Copper and Brass and 4 different S components.

The recrystallized area fraction in the P-layers was determined from the BSE images using the line intercept method and is plotted as a function of ARB cycles in Fig. 4. While after 1 ARB cycle slightly less than half of

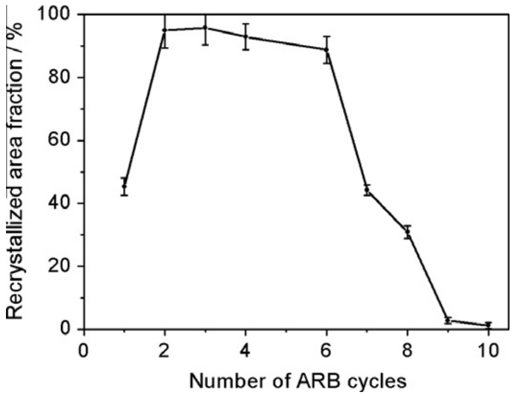

Fig. 4. Recrystallized area fraction in the P-layers as a function of ARB cycles.

the area is recrystallized, it is about 95% after 2 cycles. With further processing the recrystallized fraction stays at this high level and slightly decreases to 89% after 6 ARB cycles. A significant decrease takes place from the 7th cycle on. After 9 cycles recrystallization almost completely ceases in the P-layers.

While the A- and P-layers can be distinguished easily in the BSE images (Fig. 2c–g), in the EBSD mappings they can only be separated systematically by a subdivision according to grain size. This method yields good results for texture data, but cannot be used for grain size determination, because especially after higher ARB cycles the biggest grains in the A-layers and the smallest in the P-layers overlap in their grain size. Hence, to determine the grain size of the recrystallized grains (only) in the P-layers in ND, TD and RD the line intercept method using the BSE images was applied (Fig. 5a). It is a disadvantage of the "manual" line intercept method that very small recrystallized grains, which can hardly be distinguished from subgrains in the deformed (unrecrystallized) areas, may be overlooked. The error bars in Fig. 5a only give the systematic error. The dotted line marks the theoretical layer thickness during ARB assuming an uniform reduction of A- and P-layers.

Up to 3 cycles the grain size in ND is nearly constant at about 54 μm. After 4 cycles it decreases to 37 μm. During further processing most of the grains reach their spatial limit in ND, which is the layer thickness (Fig. 2e–g). After 9 cycles, a grain size in ND of 2.7 μm is reached, which actually significantly exceeds the theoretical layer thickness of about 2 μm. After 10 ARB cycles not enough grains could be detected for sufficient statistics. The grain sizes in TD and RD develop nearly equally. From the 1st to the 2nd ARB cycle the grain size increases from 79 to 111 μm. Up to the 6th cycle it decreases slightly to 85 μm. During further processing the grain size in RD significantly decreases to 10 μm after 9 ARB cycles. The aspect ratio, defined as the quotient of the grain size in RD and ND (Fig. 5b), is about 2 after the 2nd cycle, increases steadily to a maximum of almost 8 after the 8th cycle and abruptly drops to less than 4 during the 9th cycle. The structure of the P-layers after 6 and 7 cycles in the TD plane can be seen in the EBSD mapping in Fig. 6.

The orientation contrast in Fig. 6a and c indicates that in the P-layers the Cube and Rotated Goss (RG) component dominate in the unrecrystallized as well as in the recrystallized grains. Note that the A-layers preferentially display grains in S, Copper (Cu) and Brass (Bs) orientations. Fig. 6b and d show the same EBSD mapping with high-angle grain boundaries (HAGBs, >15°) in red and low-angle grain boundaries (LAGBs, 3–15°) in blue. Although it is not possible to make a correct subdivision of the different layers to give a disorientation distribution only in the P-layers, it can be seen in Fig. 6b and d that in the unrecrystallized areas of the P-layers almost only LAGBs are present, while most of the boundaries between recrystallized and unrecrystallized grains are HAGBs.

3.2. Texture

The results of the global texture measurements are presented as ODF sections with $\varphi_2 = 0°$ and $\varphi_2 = 45°$ (Fig. 8, preliminary results published previously in Ref. [28]). Key figures for the relevant texture components are given by

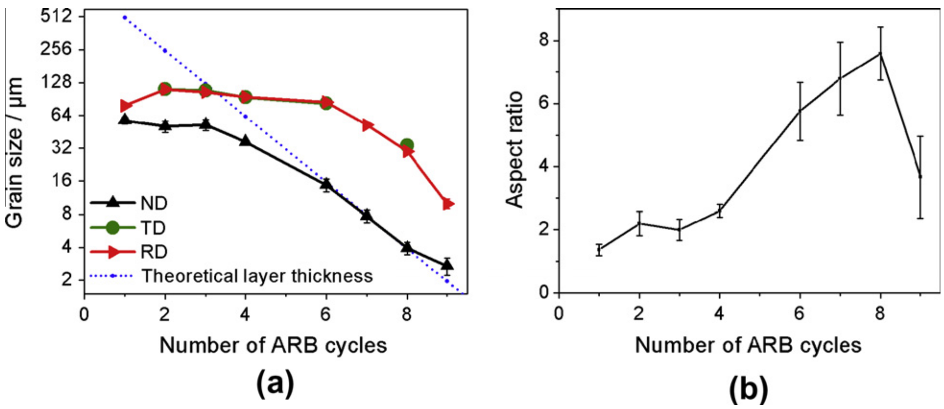

Fig. 5. (a) Grain size of the recrystallized grains in the P-layers for different directions compared with theoretical layer thickness; and (b) their aspect ratio as a function of the number of ARB cycles.

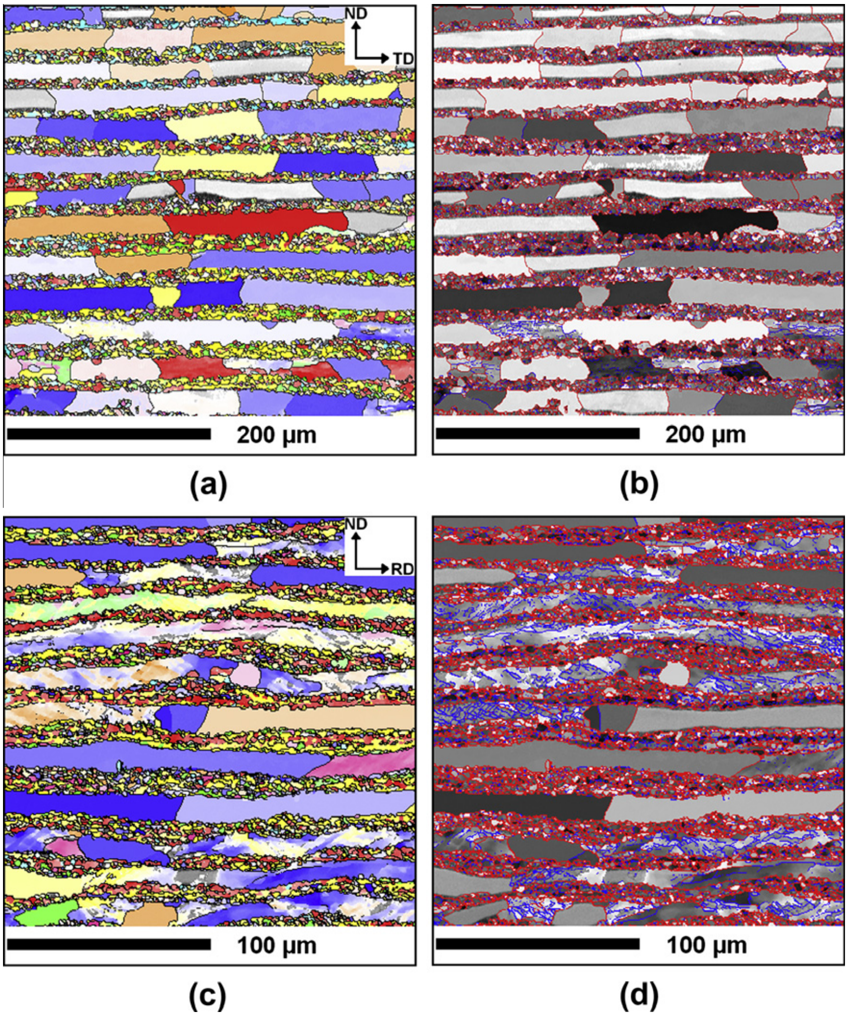

Fig. 6. (a) Orientation contrast after 6 cycles ($0.04 < s < 0.42$; step size = 1 µm) and (c) 7 cycles ($0.18 < s < 0.38$; step size = 0.5 µm). (b) and (d) show the corresponding grain boundary structure, where LAGBs and HAGBs are coloured blue and red, respectively.

Fig. 7. For the $\varphi_2 = 0°$ ODF section, monoclinic specimen symmetry is applied (Fig. 7a), which will be used later for local texture measurements on the specimen surface.

The initial materials show a strong Cube component. Additionally, the commercially pure aluminium has some remaining rolling components and a weak Goss component, while in the high-purity aluminium the Cube component shows a little spread along the ND fibre. The latter may be explained by the occurrence of some tertiary recrystallization in the high-purity sheets during annealing causing the {100} planes to become parallel to the ND plane. With increasing number of ARB cycles, the Cube component in the composite is decreasing, while rolling components (Cu, Bs and S, S only observed in $\varphi_2 = 65°$

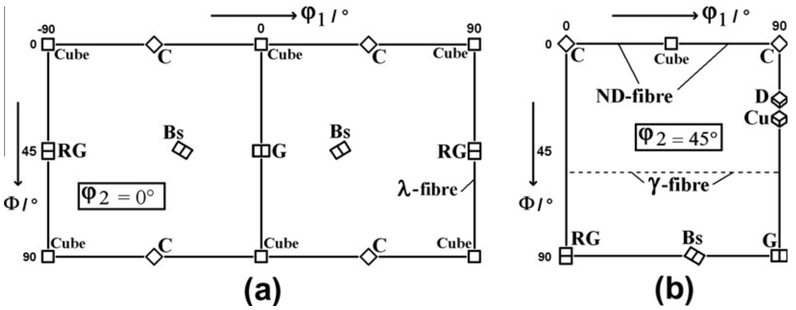

Fig. 7. Key figures for ideal orientations: (a) in the $\varphi_2 = 0°$ ODF section for monoclinic and (b) in the $\varphi_2 = 45°$ ODF section for orthorhombic specimen symmetry.

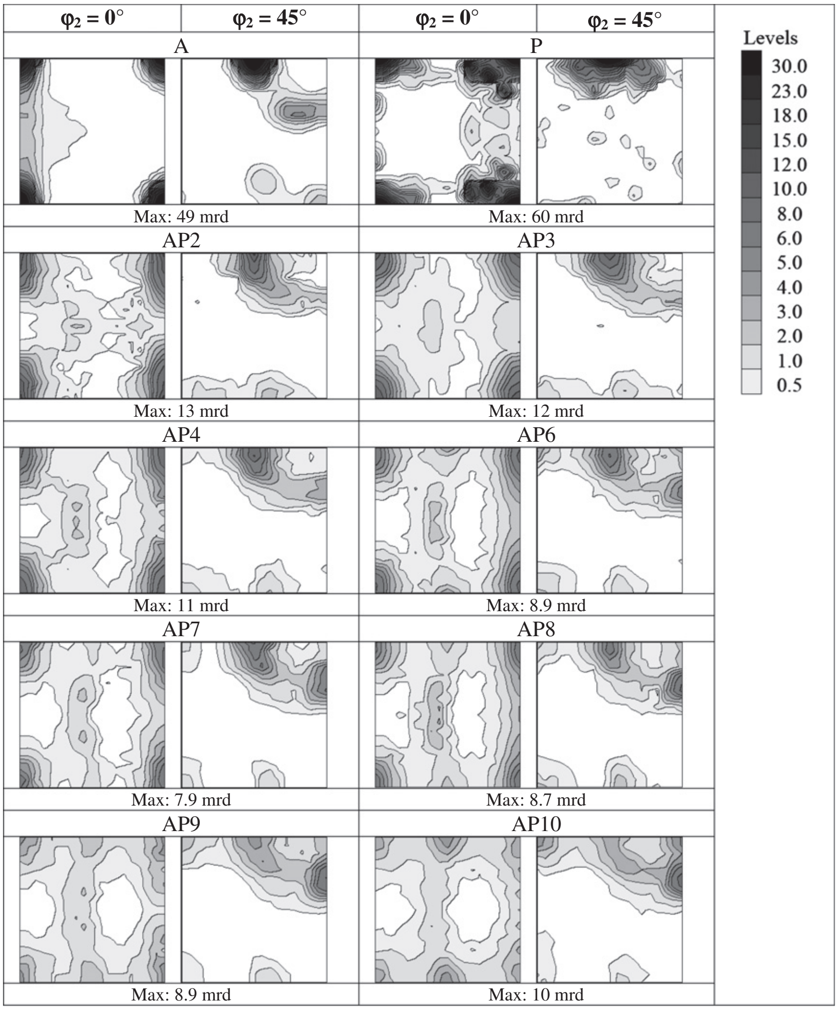

Fig. 8. Global texture of the initial materials and the composite after different ARB cycles represented by $\varphi_2 = 0°$ and $\varphi_2 = 45°$ ODF sections.

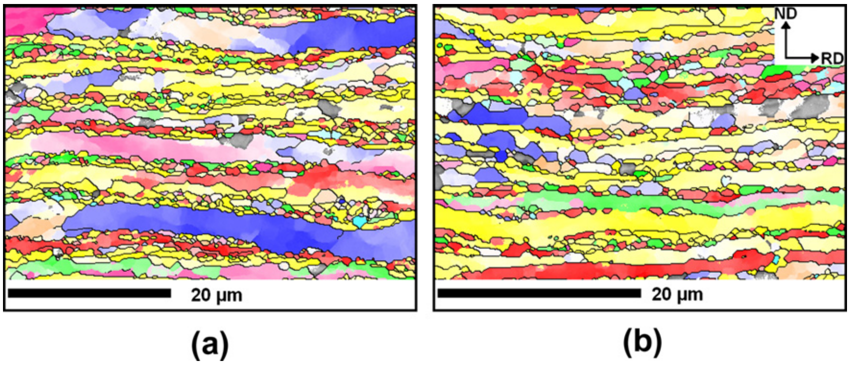

Fig. 9. Orientation contrast after (a) 9 cycles ($0.23 < s < 0.27$; step size = 0.1 µm) and (b) 10 cycles ($0.23 < s < 0.26$; step size = 0.08 µm).

ODF section) increase. The shear component Rotated Cube (C) appears after the 6th ARB cycle.

For 4 and fewer cycles the local texture from each A- and P-layer was measured by X-ray diffraction. Between the 6th and the 8th cycles, the local texture data were obtained with EBSD by separating the grains according to their grain size. Additionally, to improve the accuracy, grains were separated manually. With this method, evidence was gained easily, that, especially after 6 and 8 cycles, the rolling texture components and the C component (close to the surface) mainly originate from the A-layers, while the RG and Cube component are present in the P-layers. EBSD shows that for the highest cycle numbers the rolling components strengthen in the unrecrystallized areas of the P-layers (Fig. 9). Due to the hampered recrystallization a rolling texture develops just like in the commercially pure aluminium.

Detailed information on the development of the $\langle 100\rangle$// TD fibre, here labelled the "λ-fibre", is obtained by analyzing the local texture by X-ray measurements. These measurements were been performed on the upper surface of the sheets ($s = 0.03$) except for AP4, where it was done on the bottom surface ($s = 0.97$), because there the top has an almost 65 μm thick A-layer. The results for the $\varphi_2 = 0°$ ODF sections are presented in Fig. 10. As mentioned above, it could be proved with EBSD that after 6 cycles the components on the λ-fibre do not appear in the A-layers. It is clear that on the top of the AP6, AP7 and AP8 sheets there is a positive rotation of the Cube component around TD leading to a maximum, which is close to the ideal position of the RG component. On the bottom surface (s close to 1) the same rotation around TD takes place, but in the opposite sense, as shown in the case of AP4 (Fig. 10) and AP8 in Fig. 11. Fig. 11 shows a through-thickness evolution of this "Tilted Cube" component. At the upper surface ($s = 0.03$) there is a strong positive tilt, which already disappears at $s = 0.17$ and instead, like in the middle of the sheet ($s = 0.52$), the Cube component becomes dominant. Considering the spread around the Cube and the Tilted Cube components, the appearance of the whole λ-fibre in the global texture is understandable (Fig. 8).

4. Discussion

4.1. Microstructure development

The experimental results will be discussed below, first presuming the character of recrystallization and second

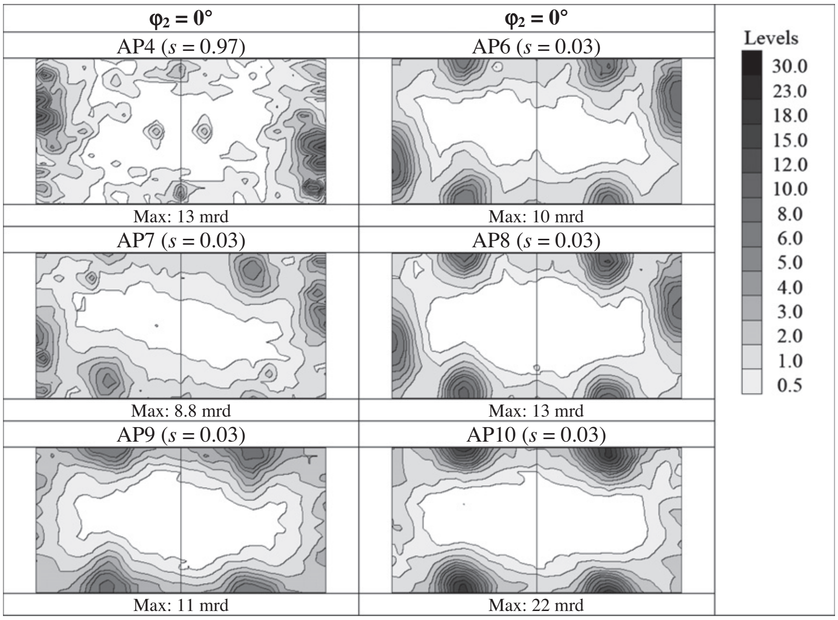

Fig. 10. Local texture close to the surface of the composite after different ARB cycles represented by $\varphi_2 = 0°$ ODF sections.

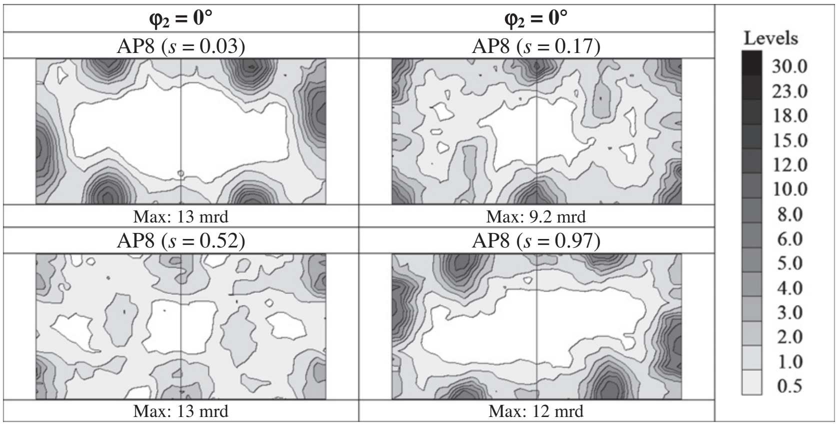

Fig. 11. Local texture of AP8 at different distances from the surface represented by $\varphi_2 = 0°$ ODF sections.

explaining the recrystallization behaviour with respect to the number of ARB cycles.

Recrystallization at ambient temperature of aluminium of very high purity has been observed previously [20,21]. Generally, due to the high stacking fault energy of aluminium dissociation of dislocations is hampered by that promoting recovery and consequently reducing the driving pressure for recrystallization. On the other hand, due to the high purity the mobility of the grain boundaries is very high, so that recrystallization already occurs at (comparatively) low temperatures and low driving pressures [29]. ARB on pure aluminium (4 N or 99.99 wt.%) has been performed previously [30], but no recrystallization in the as-deformed state could be observed. At this point it is important to note that the grain boundary mobility is very sensitive to the purity. Previous reports [22,23] show that 5 N Al dynamically recrystallizes, while 4 N aluminium only shows dynamic recovery.

There are indications that major recrystallization does not take place as discontinuous dynamic recrystallization (DDRX) but rather afterwards as a static process. In the case of sole DDRX, all recrystallized grains should have an increasingly deformed state with larger distance to the migrating grain boundary [31]. This would be visible by recovery formed subgrains subdivided by LAGBs. However no LAGBs are visible in Fig. 6, as the constant colour of the recrystallized grains shows. This can be observed even more clearly in Fig. 12, where after 8 ARB cycles the internal disorientation of the grains with respect to the orientation of their gravity centre is plotted for a range from 0° to only 1°. Considering that the casual error of the EBSD system is smaller than 1°, the recrystallized grains seem to be free of internal deformation features.

Assuming only DDRX, it is possible to estimate the minimal velocity v of the grain boundary movement necessary for the extremely elongated grains observed in RD/TD during ARB cycles 6–9. Considering the geometry of the ARB process and the parameters mentioned in the experimental details section, the upper limit of the time within which the deformation takes place is about $t_d = 0.085$ s ($\hat{=} \dot{\varepsilon}$ of at least 12 s^{-1}). Assuming a grain size of ~100 μm in RD/TD (see Fig. 6), the grain boundary has to move over a distance $d = 50$ μm. To reach the recrystallized microstructure observed (i.e. without deformation features), the migration time of the grain boundary during deformation should be much smaller than t_d, leading to the relation $v \gg d/t_d \approx 0.59$ mm s^{-1}.

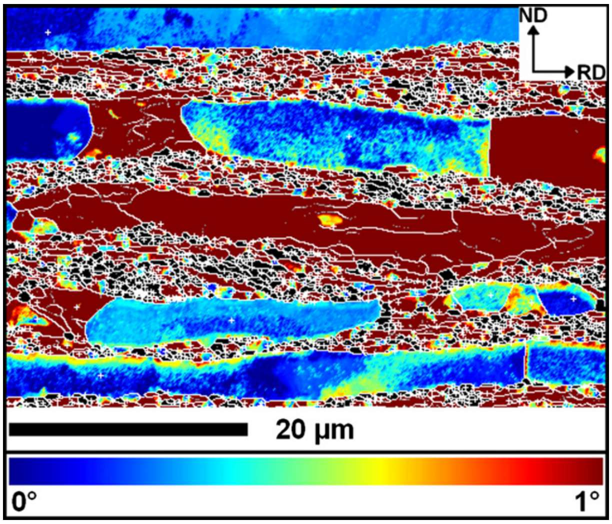

Fig. 12. Internal disorientation of the grains with respect to the orientation of their gravity centre after 8 cycles ($0.22 < s < 0.26$; step size = 0.1 μm).

Since according to own experience recrystallization of commercially pure aluminium needs time scales of minutes at comparatively high temperatures, the estimate of the velocity above of at least some cm s^{-1} is much too high. Thus, it is assumed that static recrystallization with $v \ll d/t_d$ has taken place after deformation. If the nucleation and also some growth have already taken place during deformation, this recrystallization process should be classified as metadynamic recrystallization [29]. Considering some adiabatic heating after deformation, and thereby an increase of recovery, it is reasonable to assume that most of the recrystallization has occurred within some minutes after ARB (Fig. 5).

After 1 ARB cycle less than half of the area fraction is recrystallized, in contrast to the 2nd cycle. Nucleation predominantly occurs in the interface area close to the commercially pure aluminium (Fig. 3). The grains closer to the middle of the P-layer ($s = 0.75$) seem to be inhibited in growth. This hampered recrystallization (in comparison with the 2nd cycle, where about 95% is recrystallized) may be due to a lower driving pressure for recrystallization (P_D), caused by the larger grain size of the initial high-purity sheets and a smaller interface area leading to fewer nucleation sites. The observed strong decrease of the recrystallized area fraction from the 7th cycle on should be considered as a consequence of a retarding pressure P_C on the grain boundary [15,32]. This may explain the often observed convex form of the recrystallized grains at the interface with unrecrystallized areas in Fig. 6. P_C is given by the Gibbs–Thomson relationship [29]:

$$P_c = \frac{2\gamma}{R}, \tag{1}$$

where γ is the specific interface energy of the migrating grain boundary and R is the radius of the grain boundary curvature, here proportional to the thickness of the P-layers. While γ does not change, R decreases by a factor 2 with each ARB cycle if for simplification a perfectly round curvature of the migrating grain boundary is assumed. The changes in P_D should not be essential considering the almost complete recrystallization after the 2nd and up to the 6th cycle. It is therefore expected that after a certain number of ARB cycles P_C will have reached a value close to P_D, thus preventing grain boundary movement. This supposition is coherent with the observed grain size in

ND after 9 cycles (Fig. 5a). As the variation of the layer thickness increases with higher number of cycles, a lower P_C would be expected in the thicker layer parts (if the difference in deformation does not balance it). Hence, recrystallization would be favoured in the thicker parts, leading to slightly larger grains as observed after 9 cycles.

It is noteworthy that after 7 and 8 cycles the unrecrystallized areas generally are not thinner than the theoretical layer thickness. Moreover, the change from the recrystallized to the deformed state is not very sharp, but rather takes place continuously from the 7th to the 9th cycle. Such a development may be caused by a spread in the driving pressure, e.g. due to the orientation dependence of the stored energy [33,34]. One more reason for this result may be an additional spread in the velocity of the grain boundary during recrystallization, caused by the dependence of its mobility on the disorientation angle between a recrystallizing grain and the deformed matrix, as was observed for special grain boundaries in high-purity aluminium bicrystals [35,32]. Because concurrent recovery has taken place during and after deformation (reducing P_D), the equality between P_D and P_C could have been achieved more readily for grain boundaries with lower velocity, leaving a gap of unrecrystallized P-layer.

One could argue that the nucleation rate should increase during ARB due to the increasing surface/volume ratio, leading at least to a higher number of small grains with no visible internal disorientation after a high number of cycles. However, this is not observed after 8 and more ARB cycles. Obviously, not only the movement of the grain boundaries, but also the formation of nuclei is hampered. The reason for the latter has to be the decreasing thickness of the P-layers. In Ref. [29] two mechanisms of nucleation are illustrated: strain-induced grain boundary migration (SIMB), and the model of the preformed nucleus. In the case of SIMB a pre-existing grain boundary bulges into the deformed region. To form a grain this bulge needs to exceed a critical radius, which is of the range of a few micrometers, and hence larger than the average layer thickness after 9 cycles, which is approximately 2 μm.

The model of the preformed nucleus can be considered as a discontinuous growth of subgrains in areas with high strain and orientation gradients [29]. Interestingly, the subgrain size of the deformed high-purity aluminium is also in the range of 1–2 μm (Fig. 2h). At least after 10 cycles this would lead to a two-dimensional subgrain structure in the P-layers. Thus, this nucleation mechanism would require a two-dimensional discontinuous subgrain growth, which might be energetically less favoured.

An additional reason for the hampered nucleation and grain growth could be a lower dislocation density in the unrecrystallized P-layers if the layer interface acts as a dislocation sink. This effect was observed in Ref. [15], where niobium–copper laminates produced by roll bonding were heat treated. In agreement with the present investigation, the copper layers showed grain coarsening in thick layers (19 μm) while no grain growth was found in the submicron layers. Due to recovery (higher stacking fault energy) a lower dislocation density in the present case may explain why the prevention of recrystallization is starting at a higher layer thickness of about 8 μm after the 7th cycle.

The observed microstructure is akin to that observed in Ref. [10], where statically recrystallized aluminium layers also reached the spatial limitation. However, after a sufficient annealing time the whole layer was recrystallized, while in the present work recrystallization was not complete; obviously P_D was not large enough. A broadening of the recrystallized layers due to migration into the surrounding layers as in Ref. [10] was not observed in the present investigation.

4.2. Texture formation

It is well known that the Cube component is a typical recrystallization component in rolled fcc metals [36]. However, in the present investigation, close to the surface this component is rotated around TD by 20–35°, sometimes even reaching the RG orientation.

This tilt on the surface is caused by the shear deformation [21], which during ARB takes place on the surface [37]. The friction between rolls and sheet generates shear acting in the rolling plane in RD. To investigate the shearing of an initial Cube component, the evolution of an artificial Cube texture with a 10° spread (full width at half maximum of 10°) was simulated with the viscoplastic Taylor model [38]. Only octahedral glide was considered and the strain-rate sensitivity was 0.05. Fig. 13 shows the simulation results in two Euler space sections, $\varphi_2 = 0°$ (Fig. 13a) and $\varphi_1 = 90°$ (Fig. 13b). The initial artificial texture is plotted by the coloured lines while the simulated texture is shown by the filled isolines. The rotation field corresponding to simple shear due to friction is also superimposed (black arrows); for more details on the rotation field see, for instance, Ref. [39]. Interestingly, even with a spread of 10°, the Cube orientation rotates as a whole around TD (along the λ-fibre). In fact, the real amount of applied shear on the surface is unknown, but a shear of 0.5 would cause a tilt of the Cube component in the simulated texture of about 28° (Fig. 13a), which corresponds to the maximum observed experimentally. However, no Cube and RG component are visible in the simulation: the spread is only around the Tilted Cube component, not along the whole λ-fibre. To explain the spread along the λ-fibre observed in experiment it is assumed, that the nucleation time also has a spread. Nuclei in a Cube orientation formed at the beginning of deformation (especially in areas which did not recrystallize in the previous ARB cycle) experience more rotation (tilt) due to shear than nuclei formed at the end of deformation. The first achieve a tilt in the range of the RG component or even higher, while the latter explain the remaining Cube component. Subsequent static growth of those nuclei making up the essential part of the P-layers determines the measured texture on the surface. Keeping the same reference system to study the bottom part of

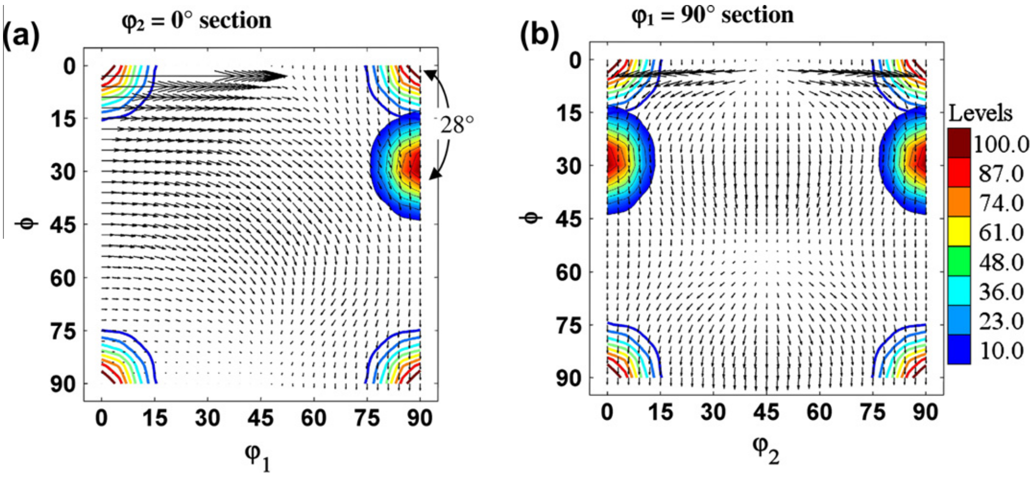

Fig. 13. Velocity field represented by black arrows corresponding to simple shear in the rolling plane in RD in the (a) $\varphi_2 = 0°$ and (b) $\varphi_1 = 90°$ ODF section. Initial Cube texture with a spread of 10° is shown by the coloured lines, the simulated texture by the filled isolines.

the sheet, the shear sense becomes inverted, leading to the opposite texture rotation, as observed at $s = 0.97$ of the AP4 and AP8 samples in Figs. 10 and 11, respectively. As shear during rolling takes place right on the surface [40], the absence of the tilt of the Cube component at $s = 0.17$ and $s = 0.52$ in Fig. 11 can be understood. The shear texture in the middle of the sheet inserted in the previous ARB cycle is obviously not stable during the subsequent cycle. After the 9th and 10th cycles, this process does not continue due to confined recrystallization. Texture changes with additional deformation lead to weaker intensity along the λ-fibre and stronger stable shear components. In particular after 10 cycles on the surface a strong C and weaker $\langle 111\rangle$//ND fibre texture (often labelled as γ-fibre) is observed (the latter is visible in the $\varphi_2 = 45°$ ODF section, not presented here).

Texture components with deviation from the λ-fibre rotate away from it towards the rolling texture components or shear components on the surface, so that after 9 and 10 cycles a fading of the λ-fibre occurs (Fig. 10).

5. Conclusions

The present work examines the microstructure and texture development of high-purity aluminium under spatial confinement during ARB. The main results of the present investigation lead to the following conclusions:

1. A composite of parallel aligned layers of commercially pure and high-purity aluminium can be produced by ARB.
2. In the high-purity aluminium metadynamic recrystallization occurs, while in the unrecrystallized areas recovery leads to a cellular subgrain structure.
3. The limited growth in ND causes large aspect ratios of the grains.
4. With the exception of the first few ARB cycles, the recrystallized area fraction decreases monotonously with decreasing layer thickness.
5. After 9 and 10 cycles, in the thinnest layers, grain growth as well as nucleation of new grains ceases.
6. Recrystallization leads to a typical Cube texture which due to shear at the surface is tilted towards RD.
7. As soon as recrystallization is confined, similar to the commercially pure aluminium the high purity aluminium develops a rolling and shear texture in the middle and at the surface of the sheet, respectively.

Acknowledgments

This work has been supported by the European Union and the Free State of Saxony in the framework of the European Centre for Emerging Materials and Processes (ECEMP), Contract No. 13795/2379. B.B. is grateful to the Alexander von Humboldt Foundation for his research fellowship.

References

[1] Saito Y, Tsuji N, Utsunomiya H, Sakai T, Hong RG. Scripta Mater 1998;39:1221.
[2] Saito Y, Utsunomiya H, Tsuji N, Sakai T. Acta Mater 1999;47:579.
[3] Tsuji N, Saito Y, Utsunomiya H, Tanigawa S. Scripta Mater 1999;40:795.
[4] Höppel HW, May J, Göken M. Adv Eng Mater 2004;6:781.
[5] Huang X, Tsuji N, Hansen N, Minamino Y. Mater Sci Eng A 2003;340:265.
[6] Scharnweber J, Skrotzki W, Oertel C-G, Brokmeier H-G, Höppel HW, Topic I, et al. Adv Eng Mater 2010;12:989.
[7] Hebert RJ, Perepezko JH. Scripta Mater 2004;50:807.
[8] Chen MC, Hsieh HC, Wu W. J Alloys Comp 2006;416:169.
[9] Min G, Lee JM, Kang SB, Kim HW. Mater Lett 2006;60:3255.
[10] Quadir MZ, Al-Buhamad O, Bassman L, Ferry M. Acta Mater 2007;55:5438.

[11] Quadir MZ, Ferry M, Al-Buhamad O, Munroe PR. Acta Mater 2009;57:29.
[12] Ohsaki S, Kato S, Tsuji N, Ohkubo T, Hono K. Acta Mater 2007;55:2885.
[13] Eizadjou M, Kazemi Talachi A, Danesh Manesh H, Shakur Shahabi H, Janghorban K. Compos Sci Technol 2008;68:2003.
[14] Quadir MZ, Al-Buhamad O, Lau KD, Quarfoth R, Bassman L, Munroe PR, et al. Int J Mat Res (formerly Z Metallkd) 2009;100:1705.
[15] Lim SCV, Rollett AD. Mater Sci Eng A 2009;520:189.
[16] Chang H, Zheng MY, Gan WM, Wu K, Maawad E, Brokmeier H-G. Scripta Mater 2009;61:717.
[17] Wu K, Chang H, Maawad E, Gan WM, Brokmeier H-G, Zheng MY. Mater Sci Eng A 2010;527:3073.
[18] Yang D, Cizek P, Hodgson P, Wen C. Scripta Mater 2010;62:321.
[19] Mozaffari A, Danesh Manesh H, Janghorban K. J Alloys Comp 2010;489:103.
[20] Kassner ME, McQueen HJ, Pollard J, Evangelista E, Cerri E. Scripta Met Mater 1994;31:1331.
[21] Skrotzki W, Scheerbaum N, Oertel C-G, Brokmeier H-G, Suwas S, Tóth LS. Acta Mater 2007;55:2211.
[22] Yamagata H. Acta Met Mater 1995;43:723.
[23] Ponge D, Bredehiifi M, Gottstein G. Scripta Mater 1997;37:1769.
[24] Beausir B, Chekhonin P, Scharnweber J, Oertel C-G, Hausöl T, Höppel HW, Skrotzki W. Acta Mater, in preparation.
[25] Beausir B, Fundenberger JJ. Software for orientation image mapping. <http://benoitbeausir:free:fr>.
[26] Brokmeier H-G. Physica B 1997;234–236:977.
[27] Beausir B, Scharnweber J, Jaschinski J, Brokmeier H-G, Oertel C-G, Skrotzki W. Mater Sci Eng A 2010;527:3271.
[28] Chekhonin P, Beausir B, Scharnweber J, Oertel C-G, Jaschinski J, Hausöl T, et al. Mater Sci Forum 2012;702–703:151.
[29] Humphreys FJ, Hatherly M. Recrystallization and related annealing phenomena. 2nd ed. Oxford: Elsevier; 2004.
[30] Kamikawa N, Tsuji N, Huang X, Hansen N. Acta Mater 2006;54:3055.
[31] Sandström R, Lagneborg R. Scripta Metall 1975;9:59.
[32] Gottstein G, Shvindlerman LS. Grain boundary migration in metals: thermodynamics, kinetics, applications. 2nd ed. Boca Raton, FL: CRC Press; 2010.
[33] Dillamore IL, Morris PL, Smith CJE, Hutchinson WB. Proc R Soc Lond A 1972;329:405.
[34] Every RL, Hatherly M. Texture 1974;1:183.
[35] Molodov DA, Czubayko U, Gottstein G, Shvindlerman LS. Scripta Met Mater 1995;32:529.
[36] Wassermann G. Texturen metallischer Werkstoffe. 2nd ed. Berlin: Springer Verlag; 1962.
[37] Lee SH, Saito Y, Tsuji N, Utsunomiya H, Sakai T. Scripta Mater 2002;46:281.
[38] Hutchinson JW. Proc Royal Soc Lond A 1976;348:101.
[39] Arzaghi M, Beausir B, Tóth LS. Acta Mater 2009;57:2440.
[40] Truszkowski W, Król J, Major B. Metall Mater Trans A 1982;13:665.